Study on thermal-hydraulic characteristics of novel channels for printed circuit heat exchanger using supercritical CO_2

He Yang[1], Jinduo Li[1], Huimin Wei[1], Xiaoze Du[2,1†], Hongwei Wu[3]

1 Key Laboratory of Power Station Energy Transfer Conversion and System (North China Electric Power University), Ministry of Education, Beijing 102206, China

2 School of Energy and Power Engineering, Lanzhou University of Technology, Lanzhou 730050, China

3 School of Physics, Engineering and Computer Science, University of Hertfordshire, Hatfield, AL109AB, UK

Abstract

Two new types of PCHE channels are proposed based on the typical airfoil fin PCHE channel proposed in literatures (standard channel) to further improve the thermal-hydraulic performances of airfoil fin PCHE channel. The small shuttle fins and oval fins are employed between the adjacent two airfoil fins of two novel channels, respectively. Using supercritical CO_2 as the working fluid, the thermal-hydraulic performances and enhancement mechanisms of the novel channels are numerically investigated. The results show that the channel with shuttle fins has the best comprehensive performance. The Nusselt number of the channel with shuttle fins is 6.7–26% larger, and the *f* factor is 8.3–18.6% larger than that of the standard channel under the selected conditions, which leads to a 3–19.1% increase in the PEC (comprehensive performance evaluation criteria).

† Corresponding author. Tel.: +86(10)61773923; Fax: +86(10)61773877. Email address: duxz@ncepu.edu.cn (X. Du)

The Nusselt number of the channel with oval fins is 9–27.3% larger, and the f factor is 26.6–43.4% larger than that of the standard channel, which leads to a 1–15.3% increase in the PEC. The applications of small fins between the adjacent two fins can effectively reduce the low-velocity region area and enhance the local disturbance, thereby effectively improving the thermal-hydraulic performance. The enhancement mechanism of the novel fin PCHE channel structure can be well explained by the principle of field synergy. It can be found that the synergies of the temperature gradient field and the velocity field in two novel channels are significantly improved.

Nomenclature

c_p specific heat capacity, J kg^{-1}K^{-1}

D_h hydraulic diameter, m

f Fanning friction factor

Fc field synergy number

h heat transfer coefficient, W m^{-2} K^{-1}

H height of model, m

L length of model, m

L_f length of airfoil fin, m

L_h horizontal pitch, m

L_s staggered pitch, m

L_{sf} length of small fin, m

L_t thickness of airfoil fin, m

L_v vertical pitch, m

Nu Nusselt number

Pr Prandtl number

p pressure, MPa

P perimeter of model, m

PEC   comprehensive performance evaluation criteria

$\dot{q}$ heat flux, W m^{-2}

Re Reynold number

S surface area, m^2

T temperature, K

$\nabla \bar{T}$ nondimensional temperature gradient

u velocity, m s^{-1}

$\bar{U}$ nondimensional velocity vector

W width of model, m

V volume of model, m^3

X active flow length, m

Greek symbols

β field synergy angle between fluid velocity and temperature gradient, °

ρ density, kg m^{-3}

Φ energy dissipation due to viscosity, W m^{-2}

μ dynamic viscosity, Pa s

μ_t turbulence viscosity, Pa s

λ thermal conductivity, W m^{-1} K^{-1}

Subscripts

bulk   fluid bulk

cold   cold-side

e   element channel

f   airfoil fin

hot   hot-side

in   inlet

L   local plane

out   outlet

s   standard channel structure

sf   small fin

wall   wall

x, y, z   x, y, z-directions

1. Introduction

In the concentrated solar power (CSP) plants, the development of supercritical carbon dioxide (s-CO_2) Brayton power cycle is one of the effective ways to improve system efficiency and reduce power generation costs [1,2]. The s-CO_2 Brayton cycle is also the promising power system for the advanced biomass power conversion systems [3,4] and the fourth-generation nuclear reactors [5,6]. As one of the vital components in s-CO_2 Brayton cycle, heat exchangers have a significant influence on the efficiency and compactness of the whole system. Due to its compact structure, as well as its high heat effectiveness and reliability under high temperature and pressure, the printed circuit heat exchanger (PCHE), as one of the most promising candidates for s-CO_2 Brayton cycle heat exchangers, has been gradually applied to various industrial fields, including that of solar energy [7], floating liquefied natural gas (FLNG) [8] and sodium-cooled fast reactors (SFRs) [9].

There are four types of PCHE channel structures involved in previous researches, i.e., straight channel, zigzag channel, S-shaped channel and airfoil fin channel. For the straight channel structure, Jeon et al. [10] investigated numerically the effect of the geometrical factors on its thermal performance. The results showed that the thermal performance of PCHE decreases monotonically with the increase of channel size. Liu et al. [11] performed theoretical and numerical studies on the fin effectiveness and the fin efficiency of PCHE. Ishizuka et al. [12] conducted the experimental study to analyze the effects of mass flow, inlet temperature and pressure on the thermal–hydraulic performance of zigzag channel PCHE. Meshram et al. [13] evaluated the performances of PCHE with straight and zigzag channels. It was found that the heat transfer coefficient of zigzag channel was higher than that of straight channel, while the pressure drop was also significantly increased. To solve this problem, Ngo et al. [14] proposed a discontinuous S-

shaped PCHE. Compared with the zigzag channel PCHE, the Nusselt number of S-shape PCHE is slightly reduced, while the pressure drop factor is greatly reduced to 20%-25% of that in zigzag PCHE.

The NACA airfoil fin channel PCHE was proposed by Kim et al. [15]. Remaining comparable total heat transfer rate per unit volume with the zigzag channel, the pressure drop of airfoil fin PCHE is only about 5% of that in the zigzag channel. The influence of the airfoil fin arrangement on heat transfer and flow resistance in PCHE channels was studied by Xu et al. [16]. The results showed that the channel with a sparser staggered arrangement of fins had an improved thermal-hydraulic performance. Kim et al. [17] also investigated numerically that the comprehensive performance of the airfoil fin PCHE was optimal when the fin completely staggered. The heat transfer performances of NACA airfoil fin channel, straight channel and zigzag channel were compared experimentally by Wang et al. [18]. The results revealed that the thermal performance of NACA airfoil fin PCHE was the best. The heat transfer correlation of molten salt in the airfoil channel was also derived.

Shi et al. [19] analyzed numerically the influences of mass flow and inlet temperature on the thermal-hydraulic performances of molten salt and s-CO$_2$ in the airfoil fin PCHE. Zhao et al. [20] studied the thermal-hydraulic performance of supercritical nitrogen in the airfoil fin PCHE through experiments and numerical simulations. The correlations of Nusselt number and friction factor of supercritical nitrogen for Reynolds number from 10000 to 14500 were obtained. The thermal-hydraulic performances of NACA 00XX series airfoil fin channel PCHEs were compared by Chen et al. [21]. It was found that the performance decrease with the airfoil thickness.

Cui et al. [22] proposed an innovative type of airfoil fin structure with better comprehensive

performance than that of NACA 0020 airfoil fin. The j factor of new fin channel can be 2.97~6.15% larger, while the pressure drop is 0~4.07% smaller. With this novel airfoil fin, Han et al. [23] carried out a study on waste heat recovery of flue gas. The experimental results showed that the effectiveness of the novel airfoil fin PCHE can reach more than 96%. Zhang et al. [24] conducted a study experimentally and numerically on a novel airfoil fin PCHE with 100 kW class heat transfer capacity. The results showed that the pressure drop in the novel airfoil fin PCHE is only about 1/6 of that in the zigzag channel PCHE at the comparative heat transfer rate.

In terms of heat transfer enhancement, Guo et al. [25] proposed the field synergy theory, which defined the field synergy angle to evaluate the synergy between the velocity field and the temperature gradient field, to explain the enhanced mechanism of convective heat transfer. The field synergy theory has been widely used in single-phase heat transfer enhancement mechanism studies [26-30].

For the s-CO_2 Brayton cycle, it is generally accepted that the effectiveness improvement of the heat exchanger leads to the increase of the cycle efficiency [31]. Under the given pumping power and the same boundary conditions, the proposed PCHE channel structure with higher thermal hydraulic performance would improve the effectiveness of the heat exchanger, so as to improve the heat engine efficiency of the sCO2 Brayton cycle. Based on the airfoil fin PCHE of Cui et al. [22], two innovative airfoil fin PCHE channels are proposed in this study. The local and overall thermal-hydraulic performances of two novel channels are analyzed with numerical simulation. With the similar PCHE physical model and boundary conditions in Kim et al. [15] and Cui et al. [22], it is proved that the thermal hydraulic performances of the two novel PCHE channel structures proposed in this study are enhanced compared with that in Cui et al. [22]. In the present study, the heat transfer performances are also investigated and discussed with the principle of field synergy. This study may be of reference

value for the optimization design of airfoil PCHE channel structure.

## 2. Concept design and physical model

2.1 Basic physical model

In the previous studies, the symmetrical NACA 0020 airfoil fin channel is one of the most widely used channel in PCHE. Then, Cui et al. [22] proposed a novel airfoil fin with better thermal–hydraulic performance than that of the traditional NACA 0020 airfoil fins. In this study, the airfoil fins investigated by Cui et al. [22] are adopted as the representative type of fins used in PCHE, which is defined as Channel 1, as shown in Fig. 1(a). The physical model of the airfoil fin PCHE is shown in Fig. 1(b), which contains two hot fluid channels and one cold fluid channel. In this counter-flow heat exchanger, the arrangement direction of fins in cold fluid channel are opposite with that in hot fluid channels. The fluids flow from the airfoil head to the airfoil tail.
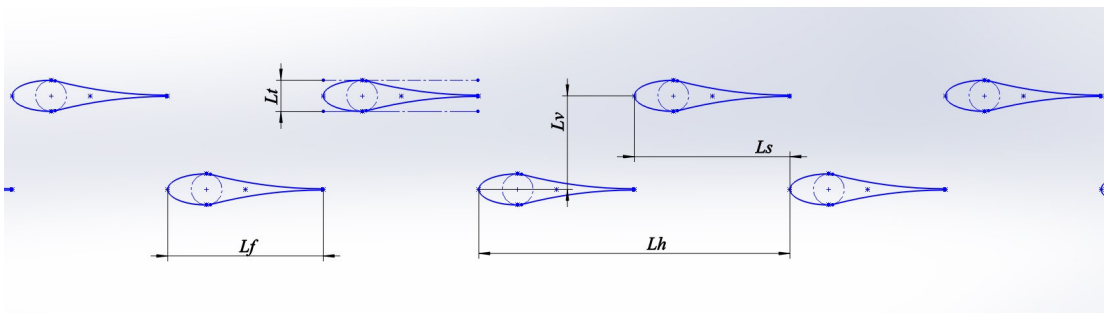
(a) Geometric parameters of airfoil fin arrangement (Channel 1).
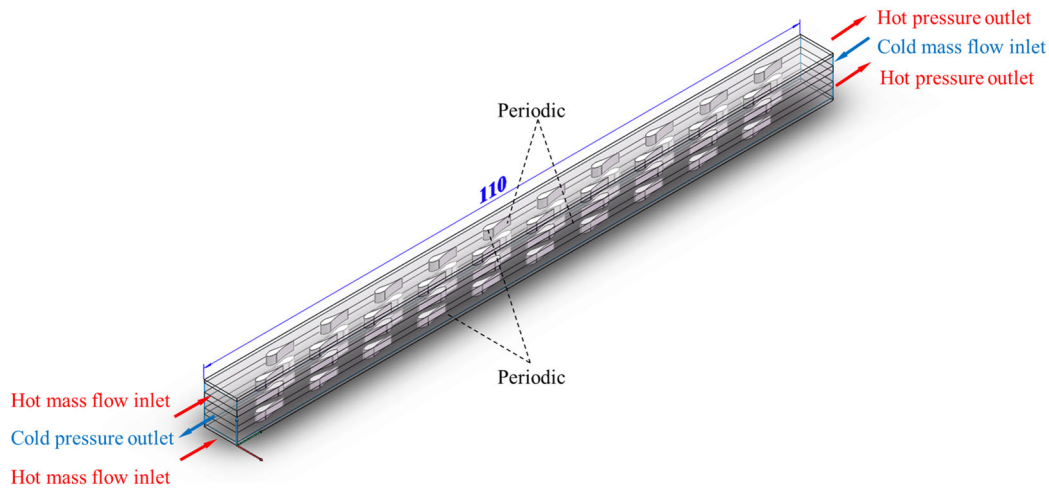
(b) Channel arrangement and configuration.
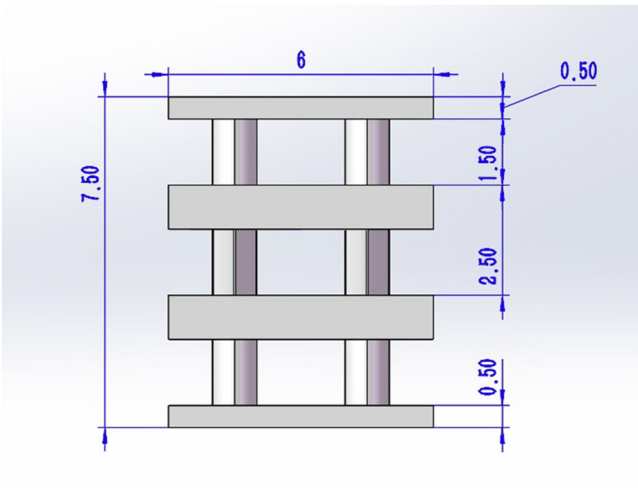
(c) Geometry and dimensions of hot and cold channels.

Fig. 1. The physical model of the airfoil fin PCHE.

For each channel, 20 airfoil fins in total are arranged completely staggered ($2L_s/L_h=1$) in two columns. The specific geometric parameters of the airfoil fins are obtained from Cui et al. [22]. As indicated in Fig. 1 (a) and (c), the overall size of the airfoil fin PCHE physical model is 110mm (L_x) × 7.5mm (L_y) × 6mm (L_z). The height of each fluid channel is 1.5mm and the height of the basic plate between the two fluid channels is 1mm. Geometric dimensions of the airfoil fins are L_f =5mm

and L_t =1mm. The arrangement parameters of the airfoil fins are L_v=3mm, L_s=5mm and L_h=10mm.

2.2 Concept design of two novel channel structures

Based on the channel configuration in Fig. 1(b), s-CO$_2$ of the cold-side channel is heated by the s-CO$_2$ of the hot-side channels. Fig. 2 shows the velocity and temperature fields of the cold-side s-CO$_2$ in Channel 1. It can be seen from Fig. 2(a) that continuous low-velocity zones are formed between every two adjacent airfoil fins by the combined effects of velocity boundary layer at the tail of fins and the coming flow strike at the head of the next fins. As the result, Fig. 2(b) shows that the thickness of the temperature boundary layer gradually increases. The cold fluid cannot directly impact the high temperature fin wall, which leads to the heat transfer performance reduction.
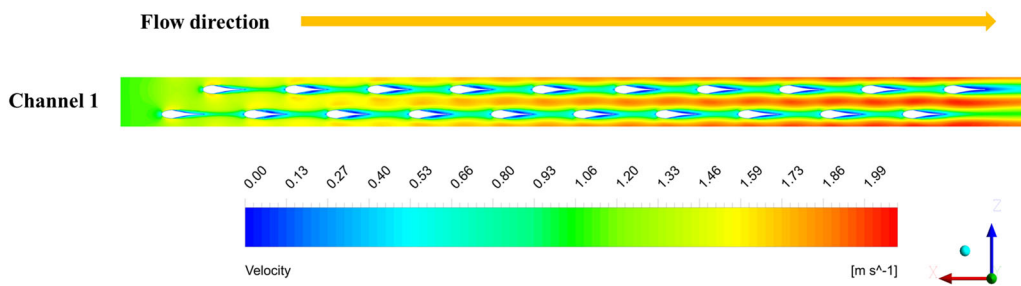

(a) Velocity.
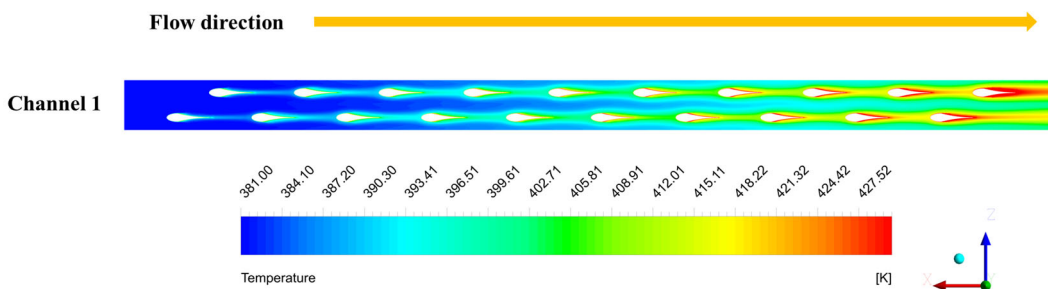
(b) Temperature.

Fig. 2. Velocity field and temperature field of s-CO$_2$ in Channel 1 (the s-CO$_2$ mass flow rate is 1.4184g/s).

Therefore, the additional fins are employed in the low-velocity region between every two adjacent airfoil fins in order to overcome the shortage in flow and heat transfer of Channel 1. The shape reference of the additional fins is taken from paper [32]. It provides the comparison of various PCHE channel structures, which are the continuous straight channel, discontinuous circular fin channel, oval fin channel and improved airfoil fin channel [16]. The Nu of the circular fin channel, oval fin channel and improved airfoil fin channel are 70.1%, 45.5% and 20.2% larger than that of straight channel, respectively. The pressure loss of the circular fin channel, oval fin channel and improved airfoil fin channel are 340%, 114% and 5.6% larger than straight channel, respectively. Among the three discontinuous channels, the improved airfoil fin that similar to rhombus-shape and shuttle-shape has the smallest resistance and the circular fin has the largest heat transfer performance. It can be seen that the employment of circular fin would improve heat transfer performance but would also bring significant increase in pressure loss. Besides, the sizes of the additional fins are restricted to be much smaller than that of airfoil fins, which can avoid an excessive increase in pressure loss. Thus, the shapes of the small fins are firstly determined to be oval, rhombus and shuttle. However, the numerical results showed that the employment of small rhombus fin would not enhance the thermal–hydraulic performance of the standard channel. Therefore, only the oval-shape and shuttle-shape small fin structures remain.

As shown in Fig. 3, two new types of PCHE channels are proposed and designed in this study. The small shuttle fins and the small oval fins are introduced between the adjacent airfoil fins, which are defined as Channel 2 and Channel 3, respectively. Channel 1 shown in Fig. 1(a) is used as the standard channel structure with only airfoil fins.
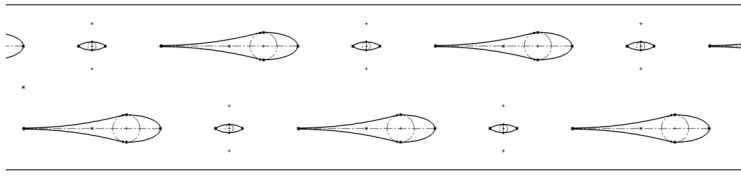
(a) Channel 2.
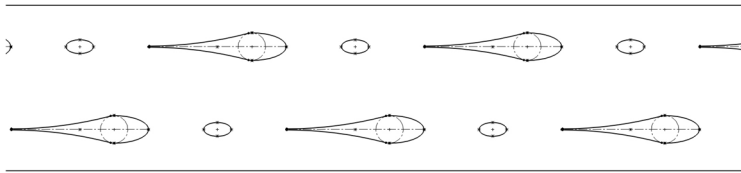
(b) Channel 3.

Fig. 3. The proposed novel PCHE channel structures.

Geometric parameters and arrangement parameters of the shuttle fins in Channel 2 are as follows. The length of shuttle fin is 1mm, the width is 0.3mm and the height is 1.5mm. Two edges of the shuttle are set to be arcs of 0.02mm in radius for the convenience of grid generation. The center of the shuttle fin is 2.5mm away from the tail of the previous airfoil and 2.5mm away from the head of the next airfoil. For Channel 3, the long axis of oval fin is 0.5mm, the short axis is 0.25mm and the height is 1.5mm. The center of the oval fin is 2.5mm away from the tail of the previous airfoil and 2.5mm away from the head of the next airfoil.

For the convenience of comparison, Channel 1 is used in all of the hot fluid channels, while three channel structures, Channel 1, Channel 2 and Channel 3, are employed in the cold channels, respectively. Owing to the shape of channel structure, the cross-sectional area varies continuously along the flow direction. The definition of airfoil fin channel hydraulic diameter proposed by Kim [17] has been widely used. Fig. 4 shows the periodic element channel adopted to calculate the hydraulic diameter, D_h, which can be hence obtained as follows.
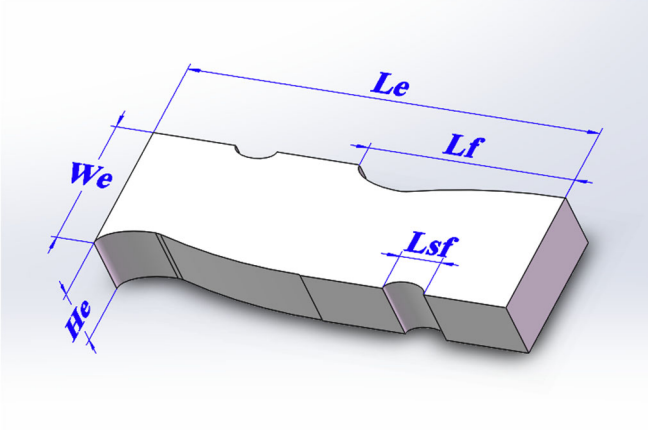
Fig. 4. Element channel for calculating the hydraulic diameter.

$$D_h = \frac{4V_e}{S_e} \tag{1}$$

$$V_e = (L_e W_e - S_f - S_{sf})H_e \tag{2}$$

$$S_e = 2\left[(P_f + P_{sf})H_e/2\right] + 2(L_e - L_f - L_{sf})H_e + 2(L_e W_e - S_f - S_{sf}) \tag{3}$$

where V_e is the volume of the element channel and S_e is the lateral area of the element channel, L_e, W_e and H_e are the length, width and height of the element channel, respectively. S_f and P_f represent the top surface area and the perimeter of the novel airfoil fin, respectively. S_{sf} and P_{sf} represent the top surface area and the perimeter of the small fin, respectively.

3. Mathematical model and numerical simulation methodology

3.1 Governing equation

The governing equations adopted in this study are as follows.

Continuity equation,

$$\frac{\partial(\rho u_i)}{\partial x_i} = 0 \tag{4}$$

Momentum Equation,

$$\frac{\partial(\rho u_i u_j)}{\partial x_j} = -\frac{\partial p_i}{\partial x_i} + \frac{\partial}{\partial x_j}\left[(\mu + \mu_t)\left(\frac{\partial u_i}{\partial x_j} + \frac{\partial u_j}{\partial x_i}\right) - \frac{2}{3}(\mu + \mu_t)\frac{\partial u_k}{\partial x_k}\right] \tag{5}$$

Energy equation,

$$\frac{\partial(\rho u_i h)}{\partial x_i} = \frac{\partial}{\partial x_i}\left[c_p\left(\frac{\mu}{Pr} + \frac{\mu_t}{Pr_t}\right)\frac{\partial T}{\partial x_i}\right] \tag{6}$$

where ρ is density, u is velocity, T is temperature, c_p is the specific heat capacity, μ is the dynamic viscosity, μ_t is the turbulence viscosity, Pr_t is the turbulent Prandtl number, $Pr_t = \frac{\mu_t c_p}{k_t} = \frac{\varepsilon_M}{\varepsilon_H}$, k_t is turbulent thermal conductivity, ε_M is momentum eddy diffusivity, ε_H is heat transfer eddy diffusivity.

It has been validated that the shear stress transport (SST) k-ω turbulence model, which combines the advantages of k-ε and k-ω models, predicts the airfoil flow characteristics well in many researches [17, 20, 22, 33, 34]. Thus, the shear stress transport (SST) k-ω turbulence model is adopted in the present computational model. The transport equations are expressed as follows.

k equation,

$$\frac{\partial(\rho k)}{\partial t} + \frac{\partial(\rho k u_i)}{\partial x_i} = \frac{\partial}{\partial x_j}\left(\Gamma_k \frac{\partial k}{\partial x_j}\right) + G_k - Y_k + S_k \tag{7}$$

ω equation,

$$\frac{\partial(\rho \omega)}{\partial t} + \frac{\partial(\rho \omega u_i)}{\partial x_i} = \frac{\partial}{\partial x_j}\left(\Gamma_\omega \frac{\partial \omega}{\partial x_j}\right) + G_\omega - Y_\omega + D_\omega + S_\omega \tag{8}$$

$$\mu_t = \rho \frac{0.31k}{max(0.31\omega, SF_2)} \tag{9}$$

$$F_2 = tanh(arg_2^2) \tag{10}$$

$$arg_2 = max\left(\frac{2\sqrt{k}}{0.09\omega y}, \frac{500\frac{\mu}{\rho}}{y^2\omega}\right) \tag{11}$$

where Γ_k and Γ_ω represent the effective diffusivities of k and ω, G_k is the production of k, G_ω is the generation of ω, Y_k and Y_ω represent the dissipations of k and ω caused by turbulence, S_k and S_ω are user-defined source terms, D_ω is cross-diffusion term. F_2 is the blending functions of the SST model. S is the magnitude of the strain rate tensor, y is the distance to the next surface.

The meshes in the near wall regions are refined to ensure that the dimensionless wall distance y^+ $\backsim 1$.

Boundary conditions,

The physical model as well as calculation domain is also indicated in Fig. 1(b). Periodic boundary conditions are employed for the top, bottom, left and right surfaces of the physical model. Coupled boundary and no-slip boundary conditions are set for the interfaces between solid and fluid domains. Besides, mass-inlet boundary conditions are imposed for the inlet of fluid regions and pressure outlet boundary conditions are set for the outlet of fluid regions. Adiabatic boundary conditions are set for the other surfaces.

The s-CO$_2$ is employed as the fluid medium for the hot and cold fluid regions. Its thermo-physical properties are derived from the NIST database [35].

The convective heat transfer coefficients of fluids in the cold and hot sides are shown as follows,

$$h = \frac{\dot{q}}{T_{\text{wall}} - T_{\text{bulk}}} \qquad (12)$$

where $\dot{q}$ represents the heat flux, T_{wall} and T_{bulk} is the wall temperature and the fluid temperature, respectively.

In addition, the Reynolds number, Re, the Nusselt number, Nu, the Prandtl number, Pr, and the Fanning friction factor, f, are shown as follows,

$$Re = \frac{\rho u D_h}{\mu} \qquad (13)$$

$$Nu = \frac{h D_h}{\lambda} \qquad (14)$$

$$Pr = \frac{\mu c_p}{\lambda} \qquad (15)$$

$$f = \frac{(p_{\text{in}} - p_{\text{out}})}{2u^2 \rho} \cdot \frac{D_h}{X} \qquad (16)$$

where μ is the dynamic viscosity, p_{in} and p_{out} means the inlet pressure and the outlet pressure, respectively. u is the average flow velocity of s-CO$_2$ in the PCHE channel, ρ is the density, and X represents the channel length.

The comprehensive thermal–hydraulic performance evaluation criteria [19], PEC, is defined as,

$$\text{PEC} = \frac{\left(\frac{Nu}{Nu_s}\right)}{\left(\frac{f}{f_s}\right)^{1/3}} \qquad (17)$$

where the subscript "s" represents the standard channel structure Channel 1. When the PEC is greater than 1, it is proved that the thermal–hydraulic performance of new PCHE channel is better than that of Channel 1.

3.2 Numerical simulation

The entire governing equations are solved in double precision by the FLUENT 2019R2 commercial software. In the computational model, the second-order upwind scheme are used for solving the momentum and energy equations, and the Coupled algorithm is employed to solve the coupling velocity and pressure. The convergence criteria for each governing equation is that all residual targets are set to be 10^{-5}.

For the channel structure of the airfoil fin PCHE is relatively complex, Fluent meshing is used to generate unstructured meshes. In order to eliminate the influence of mesh number on the numerical simulation results, five sets of meshes are established to analyze the thermal–hydraulic performance of the cold channel. Channel 1 is employed in the cold channel, where the convection heat transfer coefficient, h, and the fanning friction factor coefficient, f, are adopted in the mesh independence test.

Results of the mesh independence test are shown in Fig. 5. It can be seen that when the mesh number reaches more than 14,474,425, the relative errors of the convection heat transfer coefficient and the fanning friction factor coefficient in cold channel are within 0.3%. Thus, its mesh setting is employed in this paper. The mesh number of each fluid channel is about 3.2 million, and the mesh

number in the solid domain is about 4.8 million. In addition, the initial height of the boundary layer

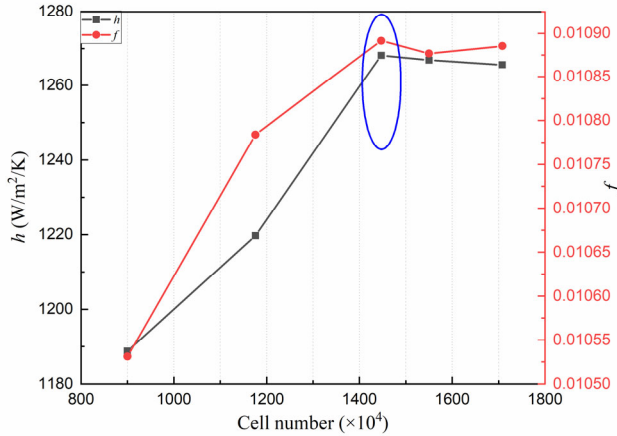in fluid domain is 0.01 mm, and the growth ratio is 1.2.

Fig. 5. Mesh independence test.

3.3 Model validation

The present numerical model is validated by the zigzag channel PCHE experimental data of

Ishizuka et al. [12]. A simplified computational model with one cold fluid channel and two hot fluid

channels is established, which structure of both cold and hot fluid channels is exactly the same with

that in Ishizuka et al.

Periodic boundary conditions are employed for the top, bottom, left and right surfaces of the

computational model as well. The hot side inlet temperature, mass flow rate and outlet pressure are

553.05K, 0.1445g/s and 2.52MPa, respectively. And the cold side inlet temperature, mass flow rate

and outlet pressure are 381.05K, 0.3152g/s, and 8.28MPa, respectively.

The comparison between the numerical results and the experimental data are shown in Table 1. It

can be seen that the relative errors of the both sides pressure difference are within 5.28%, and the

relative errors of the both sides temperature difference are within 2.92%. The results prove that the

numerical model used in this paper is accurate and appropriate.

Table 1. Numerical model validation with experimental data [12].

	Temperature difference (K)		Pressure difference (Pa)	
	Hot	Cold	Hot	Cold
Experimental results	169.6	140.38	24180	73220
Numerical results	171.09	136.28	24963	77085
Relative error (%)	0.88	2.92	3.24	5.28

4. Results with analysis

As the different structures, volumes and heat transfer areas of the three cold channels are obviously different. The heat transfer areas and hydraulic diameters of three cold fluid channels are shown in Table 2. It can be seen that the heat transfer areas of Channel 2 and Channel 3 are larger than Channel 1.

Table 2. Size data of the cold fluid channels.

Channel size parameters	Channel 1	Channel 2	Channel 3
Heat transfer area (mm^2)	1540.58	1595.83	1596.94
D_h (mm)	1.93	1.92	1.90

Mass-inlet boundary conditions are adopted in the cold-side and hot-side fluid channels. The PCHE models with three types of cold-side channels have been investigated with various cold-side inlet mass flow rates of s-CO_2, which are listed in Table 3, while the s-CO_2 mass flow rates of the hot-side channels remain constant at 0.4335g/s.

Table 3. Case data of the cold fluid channel mass flow rate and *Re*.

Case	1	2	3	4	5
Mass flow rate (g/s)	1.4184	1.6548	1.8912	2.1276	2.3640
Re number of Channel 1	15419.1	18025.8	20686.3	23320.4	25952.5
Re number of Channel 2	15450.2	18078.7	20707.2	23341.9	25974.9
Re number of Channel 3	15468.6	18111.3	20745.7	23372.2	25997.9

The inlet temperatures of both sides' channels are fixed at 553.05K and 381.05K, respectively. In addition, pressure-outlet boundary conditions are employed for both sides' channels with the constant outlet pressures of 8.28MPa at cold-side and 2.52MPa at hot-side [12, 22].

The selections of these input values are mainly to contrast the results of this paper more significantly with those of Cui et al. [22]. It would further prove that the thermal-hydraulic performances of PCHE channel structures proposed in this paper have been significantly improved compared to that of Cui et al.

4.1 Performance comparison between the three cold channels

Fig. 6 shows the thermal–hydraulic performance comparison between the three cold channels. As shown in Fig. 6(a), the Nusselt number, *Nu*, of the three channels increase with *Re*. The *Nu* of Channel 2 and Channel 3 are significantly improved compared with that of Channel 1, and Channel 3 has the largest *Nu*. As shown in Fig. 6(b), the fanning friction factor, *f*, decreases with the increase of *Re* and the *f* factor of Channel 2, Channel 3 are significantly larger than Channel 1. The *Nu*, the *f* factor of Channel 2 is 6.7–26%, 8.3–18.6% larger than that of Channel 1, respectively. The *Nu*, the *f*

factor of Channel 3 is 9–27.3%, 26.6–43.4% larger than that of Channel 1, respectively. It is obvious that the *f* factor of Channel 3 is the maximum as well. The above results show that Channel 1 has the best hydraulic performance but the worst heat transfer performance. Channel 3 has the best heat transfer performance but poor hydraulic performance. Compared with Channel 3, Channel 2 has approximate heat transfer performance but better hydraulic performance.
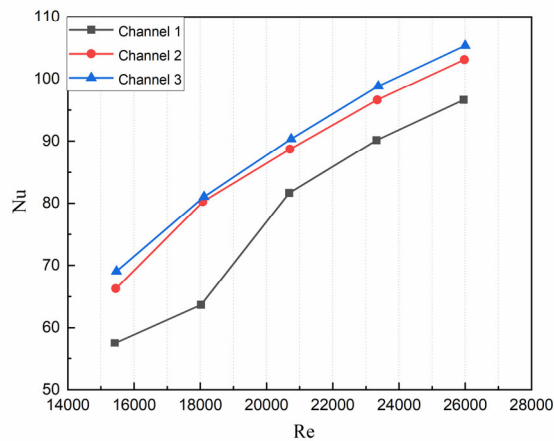
(a) Overall Nusselt number.
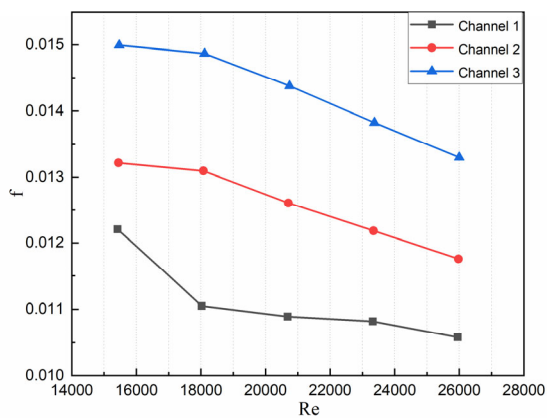
(b) Overall Fanning friction factor.
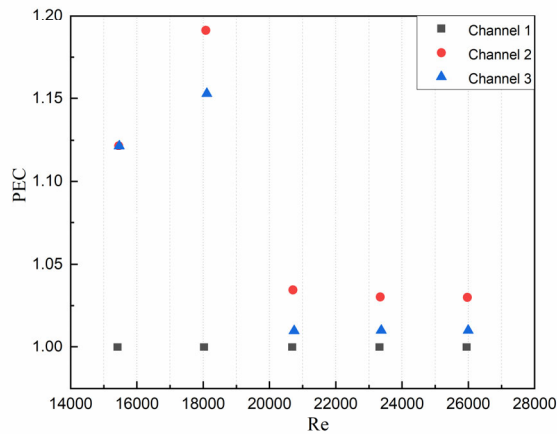
(c) Performance evaluation criterion.

Fig. 6. Overall performances of three cold fluid channels with Reynold number.

PEC is adopted to compare the comprehensive thermal–hydraulic performances of the three cold channels. As shown in Fig. 6(c), the PEC of Channel 2 and Channel 3 are greater than 1, which means that the thermal–hydraulic performances of Channel 2 and Channel 3 are better than Channel 1. Compared with Channel 1, the friction factor f and Nu of Channel 2 and Channel 3 both increase. Although the hydraulic performance of Channel 2 and Channel 3 decrease, the comprehensive performance of them are still better than Channel 1 thanks to the significant enhancements in heat transfer performances. PEC of Channel 2 and Channel 3 are 3–19.1% and 1-15.3% larger than Channel 1, respectively.
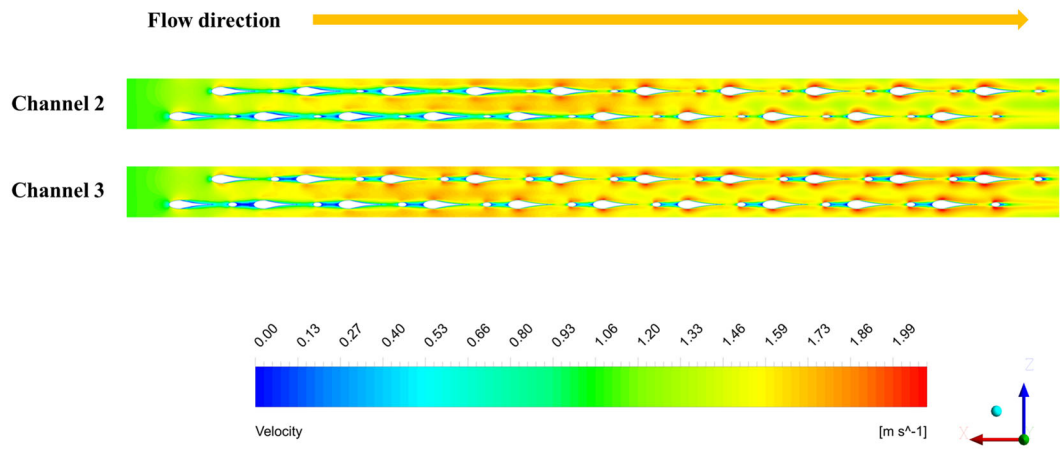
In summary, Channel 2 has the maximum PEC among the three cold channels. That is, Channel 2 has the best comprehensive thermal–hydraulic performance and is the best choice among the three channel structures.
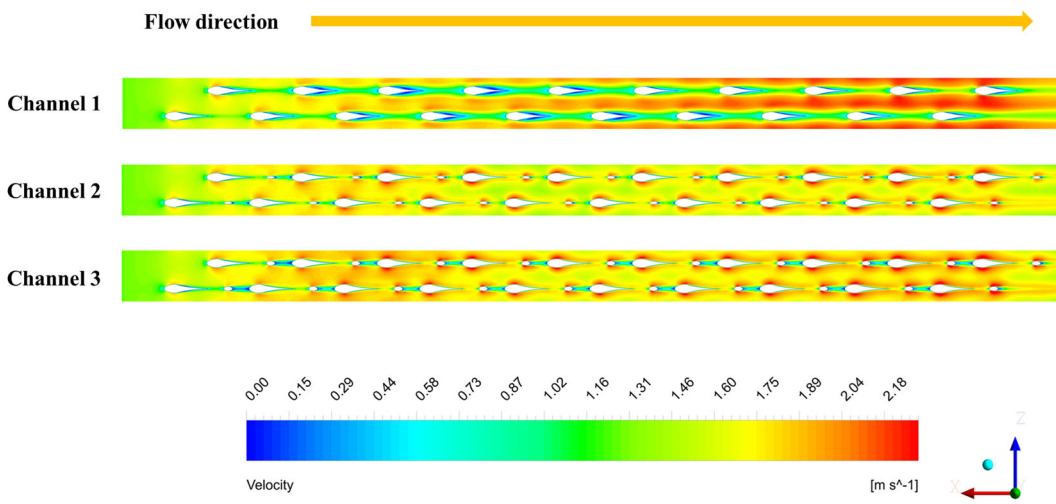
4.2 Analysis of PEC in three channels

As shown in Fig. 6(c), the enhancements of PEC are more than 10% in case1 and case2, while the PEC improvements of Channel 2 and Channel 3 in case3, case4 and case5 are only more than 3% and 1%, respectively.

Fig. 2(a), Fig. 7(a) and (b) shows the velocity distributions of the three channels under the low flow velocity of case 1 and case 2. As indicated in previous, the low-velocity regions lead to the worse heat transfer performance of Channel 1. Then, the small shuttle fins and oval fins are inserted between the front and rear airfoil fins in Channel 2 and Channel 3, respectively. Applications of the small fins lead to the fluid strikes the leading edge of the shuttle and oval fins, which enhance local disturbance and further improve heat transfer performance. Besides, since the flow area of the channels decrease, and the fluid is splitted into two parts along the small fin wall, the velocity along the both sides of the small fin increases, which leads to the total low-velocity zone area between the adjacent fins decreases significantly and the heat transfer performances of the novel channels are enhanced. In addition, due to the decrease of the low-velocity zone area, the growth in the thickness direction of boundary layer near the airfoil fin weakens, thereby further enhancing the heat transfer performance.
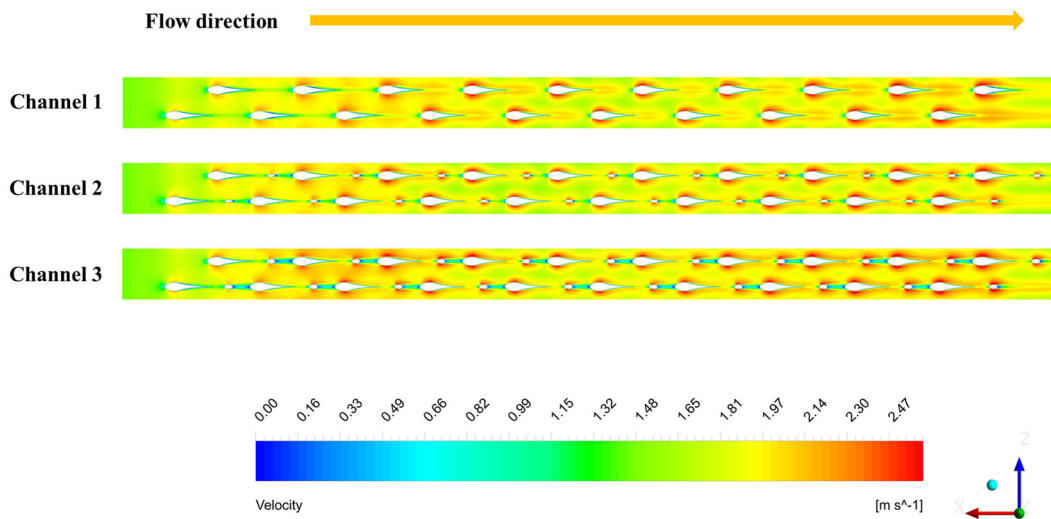
As shown in Fig. 7(a) and (b), the total areas of the low-velocity zones in Channel 2 and Channel 3 significantly decrease in case1 and case2 compared with that in Channel 1, and the heat transfer performances of two novel channels are significantly improved as well. Although the employments of small fins lead to the increase in the pressure drop, the great enhancements of heat transfer performance in Channel 2 and Channel 3 makes the PEC of these two channels increase by more than 10%.

Flow direction

Channel 2

Channel 3

0.00 0.13 0.27 0.40 0.53 0.66 0.80 0.93 1.06 1.20 1.33 1.46 1.59 1.73 1.86 1.99

Velocity [m s^-1]

(a) Case 1.

Flow direction

Channel 1

Channel 2

Channel 3

0.00 0.15 0.29 0.44 0.58 0.73 0.87 1.02 1.16 1.31 1.46 1.60 1.75 1.89 2.04 2.18
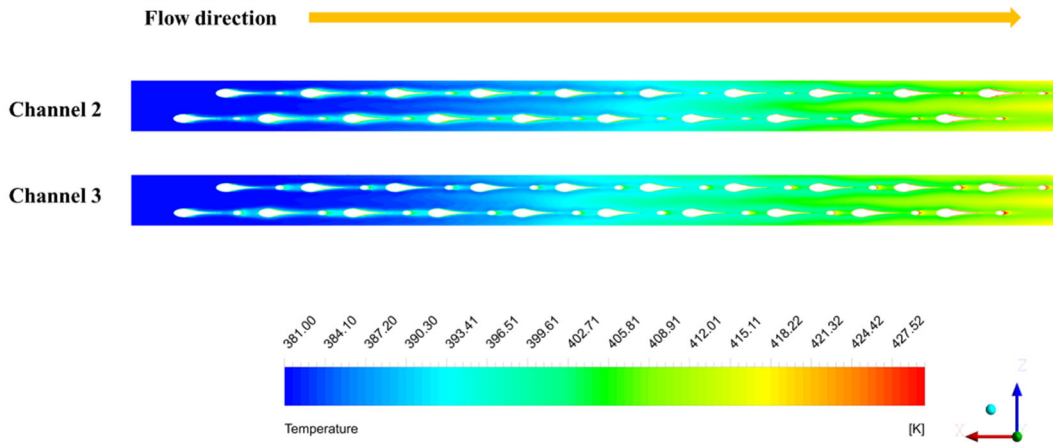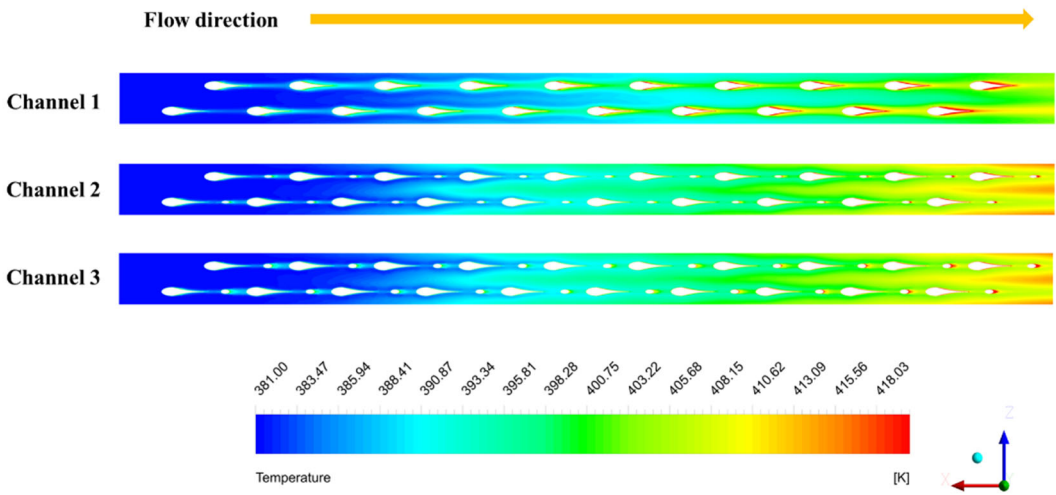
Velocity [m s^-1]

(b) Case 2.

(c) Case 3.

Fig. 7. The distributions of velocity in the three types of channels.

With the increase of mass flow rates in case 3, case 4 and case 5, the higher flow velocity makes the velocity boundary layer reduction along the airfoil fins in Channel 1. As shown in Fig. 7(c), the low-velocity zones between the two adjacent airfoil fins in Channel 1 breaks off, which means that the continuous low-velocity zone basically disappears. In these cases, the area of low-velocity zone is not significantly reduced by the applications of small fins between the every two adjacent airfoil fins. The heat transfer enhancements are mainly caused by the following two aspects, (1) the strikes of fluid with the small fins improve local disturbance to enhance heat transfer, and (2) the increase of the flow velocity along the small fins strengthens the heat transfer performance. Therefore, the enhancements of heat transfer performances in Channel 2 and Channel 3 are not as significant as that in previous cases.

(a) Case 1.

(b) Case 2.
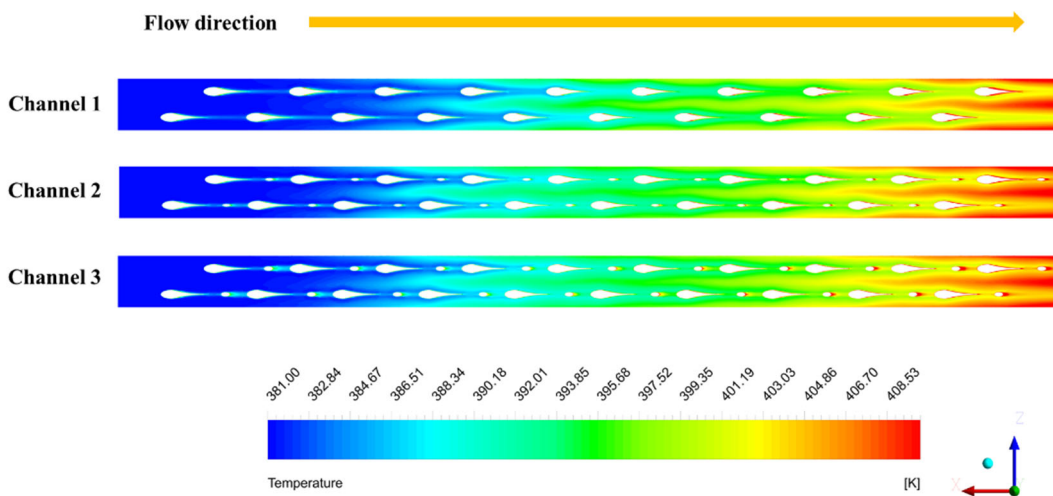
(c) Case 3.

Fig. 8. The distributions of temperature in the three types of channels.

The analysis results of temperature contours are consistent with those of the above velocity contours. Fig. 2(b), Fig. 8(a) and (b) shows the temperature distributions of the three channels under the low flow velocity of case 1 and case 2. It can be seen that the employments of small shuttle fins and oval fins lead to the significant reduction of temperature boundary layer thickness along the airfoil fin wall, and the convection heat transfer performance of the two novel channels is significantly improved.

With the increase of mass flow rates in case 3, case 4 and case 5, the temperature boundary layer decreases along the airfoil fins in Channel 1. As shown in Fig. 8(c), the thickness of temperature boundary layer along the airfoil fin wall in two novel channels decreases slightly but not as significantly as that in case 1 and case 2, so the enhancement of convective heat transfer performance is not as significant as that in the previous cases.

4.3 Analysis of local thermal-hydraulic performances

To further study the reasons of comprehensive thermal-hydraulic performance improvements in the new PCHE channels, Channel 2 and Channel 3, the local thermal-hydraulic performances of the three cold channels Channel 1, Channel 2 and Channel 3 are analyzed in details.

In order to avoid the effects of the channel inlet and outlet on the flow stability, the local zone from the leading edge of the 9th fin to that of the next one in the same column is employed to investigate the local thermal-hydraulic performance with the cold-side inlet mass flow rate is 1.8912g/s. There

are 10 equidistant cross-sectional planes established in this zone and numbered in sequence, so as to analyze the local Re, Nu and f along the flow direction. The local Reynolds number, Re_L, the local Nusselt number, Nu_L and the local Fanning friction factor, f_L, are shown as follows,

$$Re_L = \frac{\rho_L u_L D_h}{\mu_L} \qquad (18)$$

$$h_L = \frac{\dot{q}_L}{T_{\text{wall,L}} - T_{\text{bulk,L}}} \qquad (19)$$

$$Nu_L = \frac{h_L D_h}{\lambda_L} \qquad (20)$$

$$f_L = \frac{(p_{\text{in}} - p_L)}{2u_L^2 \rho_L} \cdot \frac{D_h}{X_L} \qquad (21)$$

where the $\dot{q}_L$ represents the local heat flux, $T_{\text{wall,L}}$ and $T_{\text{bulk,L}}$ represent the local wall temperature and local bulk temperature, $(p_{\text{in}} - p_L)$ means the pressure drop at the local plane, X_L means the flow length from inlet to the local plane, u_L is the average flow velocity of s-CO_2 in the local cross-sectional plane and the other parameters are obtained from the local cross-sectional plane..

As shown in Fig. 9, the local zones of the cold channels are mainly divided into three parts: the broadening part, the thinning part and the no-fin part.
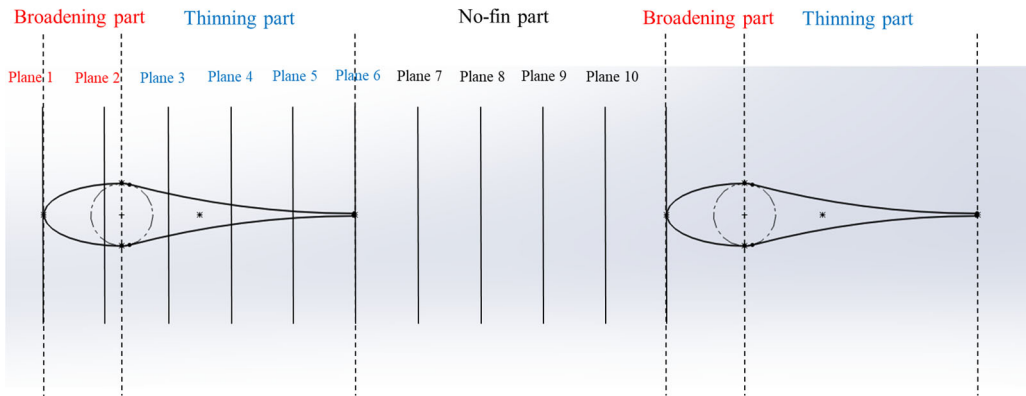

Fig. 9. The local zones of Channel 1.

Plane 1 and Plane 2 of three cold channels are located in the broadening part. Plane 3, Plane 4, Plane 5, and Plane 6 are located in the thinning part. However, the no-fin part of the local zone in

three cold channels are quite different: Plane 7, Plane 8, Plane 9, and Plane 10 in Channel 1 are all located in the no-fin part, while in Channel 2 and Channel 3 only Plane7 and Plane 10 are located in the no-fin part. The shuttle fin and oval fin are located between Plane 8 and Plane 9 in Channel 2 and Channel 3, respectively. Fig. 10 shows the distributions of local parameters at the cross-sectional planes of three cold fluid channels.
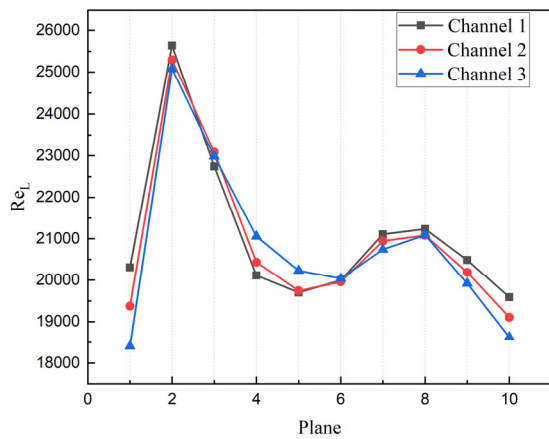
(a) Local Reynold numbers.
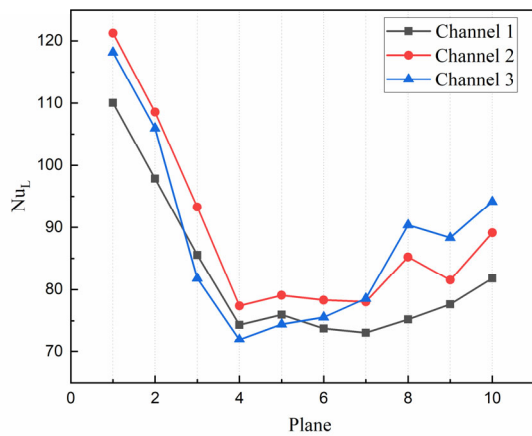
(b) Local Nusselt numbers.
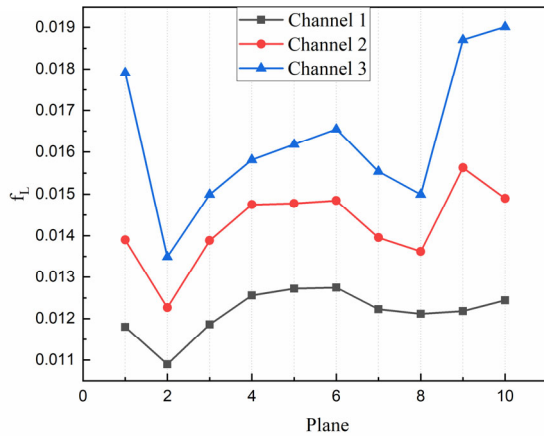
(c) Local *f* factors.

Fig. 10. The distributions of local parameters at the cross-sectional planes of three cold fluid channels.

The local Reynolds number, Re_L, distributions for three cold channels at the cross-sectional planes are shown in Fig. 10(a). The flow velocity and Re_L of the Plane 1 are relatively low due to the strike of the fluid with the fin head. With the broadening of airfoil fin, the decrease of the flow area leads to the increase of fluid velocity and Re_L. In the thinning part, the increase of flow area leads to the drop of fluid velocity and Re_L. Afterwards, in the no-fin region of Channel 1, the Re_L gradually rises since the velocity boundary layer effects gradually decrease. Then, the low velocity area caused by the next fin makes Re_L fall down again.

The overall variation trends of Re_L in Channel 2 and Channel 3 are similar to that in Channel 1. While affected by the strike of the fluid with small fin head and the velocity boundary layer at the small fin tail, Re_L of Channel 2 and 3 from Plane 7 to Plane 10 are lower than that of Channel 1.

The local Nusselt number, Nu_L, distributions for the three channels at the cross-sectional planes are shown in Fig. 10(b). The maximum Nu_L appears in Plane 1 since the coming flow impacts the

leading edge of fin, which enhances the local disturbance and disrupts the velocity boundary layer, that is, the heat transfer performance is strengthened. The flow velocity decreases along the flow direction of the airfoil fin, and the thickness of velocity boundary layer near the airfoil fin wall increases. However, the growth of velocity boundary layer in the thickness direction is not conducive to the enhancement of heat transfer performance, so that the Nu_L gradually decreases.

In the no-fin part of Channel 1, the decreasing velocity boundary layer effect results in the increase of velocity and Nu_L. In the same part of Channel 2 and Channel 3, the Nu_L are significantly larger than Channel 1. This is because the fluids in two novel channels impact the leading edges of shuttle fin and oval fin, where the further enhanced local disturbance leads to the heat transfer performance improvement. Besides, separated into two parts along the small fin wall, the flow velocity along the small fin wall increases and the low-velocity region between the two airfoils decreases. Between Plane 8 and Plane 9, the Nu_L of Channel 2 and Channel 3 decrease slightly because the boundary layers formed at the trailing edges of the small fins (Plane 9) are unfavorable to heat transfer performance.

In summary, the heat transfer performances of Channel 2 and Channel 3 are obviously enhanced. In addition, in the two novel cold channels, the local disturbance caused by the impact of fluid with oval fin is stronger than that of the shuttle fin, so that the heat transfer performance of Channel 3 is the best.

The local f factor, f_L, distributions for the three channels at the cross-sectional planes are shown in Fig. 10(c). It can be seen that the f_L of Channel 1 is the smallest, and the f_L of Channel 3 is even larger than Channel 2. This is because the two novel channels employ the shuttle fins and oval fins. The flow resistance increases in the two new channels, which leads to larger fanning friction factor

f_L than Channel 1. Compared with the oval fins of Channel 3, the head and tail of shuttle fins in Channel 2 tend to be flatter and more streamlined. The smoother transition streamline is obtained after the fluid impacts the leading edge of the shuttle fin, which brings smaller flow resistance and f_L for the shuttle fin structure.

Variations in the fin width also have a certain effect on the flow resistance. In the broadening part, as the fluid velocity increases, the velocity boundary layer near the airfoil fin decreases and the f_L gradually decreases. Then, in the thinning part of the airfoil fin, the decrease of fluid velocity results in the increase of velocity boundary layer thickness near the airfoil fin wall and the f_L gradually. In the no-fin part of Channel 1, the decreasing f_L is mainly caused by the decreasing velocity boundary layer effect. In the low-velocity zone formed by impact of the flow to the head of next airfoil fin, the f_L increases accordingly. In Channel 2 and Channel 3, the velocity boundary layer formed along the walls of shuttle fins and oval fins makes the f_L between Planes 8 and 9 increase significantly.

According to the field synergy principle [25], the expressions of the field synergy number Fc and the Nusselt number Nu are shown as follows.

$$Fc = \frac{Nu}{RePr} = \int_0^1 (\bar{U} \cdot \nabla \bar{T}) d\bar{y} \qquad (22)$$

$$Nu_L = Re_L \, Pr_L \int_0^1 (\bar{U} \cdot \nabla \bar{T}) d\bar{y} \qquad (23)$$

$$\bar{U} \cdot \nabla \bar{T} = |\bar{U}| \cdot |\nabla \bar{T}| \cos \beta \qquad (24)$$

It can be seen that the Nu is not only related to the velocity field and the temperature gradient field, but also to the synergy angle, β, between the two fields. The better synergy between the velocity field and the temperature gradient field, which means the larger cosine value of the included angle between the two fields, corresponds to the higher convective heat transfer rate under

the same other conditions. Therefore, the smaller included angle between the velocity field and the temperature gradient field can achieve the larger convective heat transfer coefficient.

Fig. 11 shows the local field synergy angles of three cold channels from Plane 1 to Plane 10. It can be seen that from Plane 7 to Plane 10, the local field synergy angle of Channel 2 is 3.4-4.6% smaller than that of Channel 1 and the local field synergy angle of Channel 3 is 4.8-12.8% smaller than that of Channel 1. The above results provide the explanation for the variations of the Nu_L in Fig. 10(b).
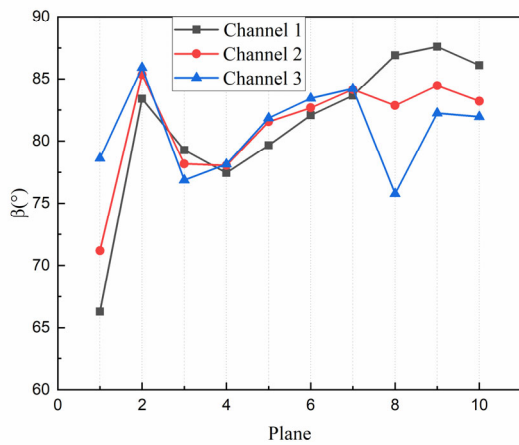

Fig. 11. Local field synergy angle of different channels.

In addition, Table 4 below shows the field synergy numbers, Fc, of the three channels in that case, where the Fc of Channel 3 is the largest and the Fc of Channel 1 is the smallest. Therefore, the shuttle fins and oval fins employed in Channel 2 and Channel 3 change the velocity field distributions between the two adjacent airfoil fins and improve the synergy between the velocity field and the temperature gradient field. Thus, the heat transfer performances of the two novel channels are strengthened.

Corresponding to the previous analysis results, Channel 3 has the best convective heat transfer performance and Channel 1 has the worst convective heat transfer performance. The field synergy principle is employed to provide the mechanism explanation for the improvements of convective heat transfer performances of the two new channels (Channel 2 and Channel 3).

Table 4. Field synergy numbers of three channels (cold-side inlet mass flow rate is 1.8912g/s).

Field synergy number	Channel 1	Channel 2	Channel 3
Fc	0.00438	0.00475	0.00483

5. Conclusions

In this present work, two novel PCHE channel structures are designed to improve the thermal-hydraulic performance of PCHE. In the research process, using s-CO_2 as the working fluid, the thermal-hydraulic performances of the two new channels are numerically studied and the enhanced heat transfer mechanisms of the new channels are analyzed and discussed. The specific conclusions are as follows.

(1) The *Nu* and *f* factor of Channel 2 are 6.7–26%, 8.3–18.6% larger than that of Channel 1, respectively. The *Nu*, the *f* factor of Channel 3 are 9–27.3%, 26.6–43.4% larger than that of Channel 1, respectively. The comprehensive performance evaluation criteria (PEC) is employed to compare the thermal–hydraulic performances of the three channels. The PEC of Channel 2 and Channel 3 are 3–19.1% and 1–15.3% larger than that of Channel 1, respectively. It can be seen that Channel 2 has the best thermal–hydraulic performance among the three channels.

(2) In case 1 and case 2, the PEC enhancements of two novel channels are more than 10%, while the PEC improvements of Channel 2 and Channel 3 in case 3, case 4 and case 5 are just more than 3%

and 1%, respectively. The reason is that under the low flow velocity conditions, the combined effects of velocity boundary layer and the coming-flow strike form a continuous low-velocity zone between the adjacent two airfoil fins, which is not conducive to the convective heat transfer. In the two novel channels, the impacts of the coming-flow formed by the employments of small fins strengthen the local disturbance and improve the heat transfer performance. In addition, the flow area between two adjacent airfoils decreases and the flow velocity along the small fins increases, so that the continuous low-velocity zone decreases significantly and heat transfer is enhanced. However, with the increase of mass flow rate, the raise of flow velocity makes the decrease of velocity boundary layer near fin wall in Channel 1, which leads to the continuous low-velocity zone breaks off gradually as well. The heat transfer enhancement effects of the two novel channels are not as significant as before.

(3) The variation trends of local Nu, Re and f in the three channels are analyzed to discuss the enhanced heat transfer mechanisms of the two new channels. Although the small fins introduced in the no-fin region (from Plane 7 to Plane 10) make the local f-factor increase, it also significantly improves the local heat transfer. According to the principle of field synergy, it can be found that the synergies of the temperature gradient field and the velocity field from Plane 7 to Plane 10 in Channel 2 and Channel 3 are significantly improved, thereby enhancing the convective heat transfer of the two new channels.

References

[1] Yang J, Yang Z, Duan Y. Off-design performance of a supercritical CO_2 Brayton cycle integrated with a solar power tower system. Energy 2020;201:117676.

[2] Yang J, Yang Z, Duan Y. A review on integrated design and off-design operation of solar power tower system with S-CO_2 Brayton cycle. Energy 2022;246:123348.

[3] Manente G, Lazzaretto A. Innovative biomass to power conversion systems based on cascaded supercritical CO_2 Brayton cycles. Biomass Bioenerg 2014;69:155-168.

[4] Cao Y, Dhahad H A, Hussen H M, ATTIA E A, Rashidi A, Shamseldin M A, Almojil S F, Almohana A I, Alali A F. Techno-economic investigation and multi-criteria optimization of a novel combined cycle based on biomass gasifier, S-CO_2 cycle, and liquefied natural gas for cold exergy usage. Sustain Energy Technol Assess 2022;52:102187.

[5] Gao C, Wu P, Shan J, Huang Y, Zhang J, Wang L. Preliminary study of system design and safety analysis methodology for supercritical carbon dioxide Brayton cycle direct-cooled reactor system. Ann Nucl Energy 2020;147:107734.

[6] Ding H, Lu D G, Sui D T, Zhang Y L. Development of transient thermal-hydraulic analysis code for SCO_2-cooled reactor coupled with Brayton cycle and its application. Ann Nucl Energy 2022;175:109255.

[7] Zhu Q, Tan X, Barari B, Caccia M, Strayer A R, Pishahang M, Sandhage K H, Henry A. Design of a 2 MW ZrC/W-based molten-salt-to-sCO2 PCHE for concentrated solar power. Appl Energ 2021;300:117313.

[8] Cai W H, Li Y, Li Q, Wang Y, Chen J. Numerical investigation on thermal–hydraulic performance of supercritical LNG in a Zigzag mini-channel of printed circuit heat exchanger. Appl Therm Eng 2022;214:118760.

[9] Lee S W, Shin S M, Chung S, Jo H. Evaluation of thermal-hydraulic performance and economics of Printed Circuit Heat Exchanger (PCHE) for recuperators of Sodium-cooled Fast Reactors (SFRs) using CO_2 and N_2 as working fluids. Nucl Eng Technol 2022;54:1874-1889.

[10] Jeon S, Baik Y, Byon C, Kim W. Thermal performance of heterogeneous PCHE for supercritical CO_2 energy cycle. Int J Heat Mass Tran 2016;102:867-876.

[11] Liu S, Huang Y, Wang J. Theoretical and numerical investigation on the fin effectiveness and the fin efficiency of printed circuit heat exchanger with straight channels. Int J Therm Sci 2018;132:558-566.

[12] Ishizuka T, Kato Y, Muto Y, Nikitin K, Lam N, Hashimoto H. Thermal-hydraulic characteristics of a printed circuit heat exchanger in a supercritical CO_2 loop. In: The 11th International Topical Meetings on Nuclear Reactor Thermal–Hydraulics, 2005.

[13] Meshram A, Jaiswal A K, Khivsara S D, Ortega J D, Ho C, Bapat R, Dutta P. Modeling and analysis of a printed circuit heat exchanger for supercritical CO_2 power cycle applications. Appl Therm Eng 2016;109:861-870.

[14] Ngo T L, Kato Y, Nikitin K, Ishizuka T. Heat transfer and pressure drop correlations of microchannel heat exchangers with S-shaped and zigzag fins for carbon dioxide cycles. Exp Therm Fluid Sci 2007;32:560-570.

[15] Kim D E, Kim M H, Cha J E, Kim S O. Numerical investigation on thermal–hydraulic performance of new printed circuit heat exchanger model. Nucl Eng Des 2008;238:3269-3276.

[16] Xu X, Ma T, Li L, Zeng M, Chen Y, Huang Y, Wang Q. Optimization of fin arrangement and channel configuration in an airfoil fin PCHE for supercritical CO2 cycle. Appl Therm Eng 2014;70:867-875.

[17] Kim T H, Kwon J G, Yoon S H, Park H S, Kim M H, Cha J E. Numerical analysis of air-foil shaped fin performance in printed circuit heat exchanger in a supercritical carbon dioxide power cycle. Nucl Eng Des 2015;288:110-118.

[18] Wang W Q, Qiu Y, He Y L, Shi H Y. Experimental study on the heat transfer performance of a molten-salt printed circuit heat exchanger with airfoil fins for concentrating solar power. Int J Heat Mass Tran 2019;135:837-846.

[19] Shi H Y, Li M J, Wang W Q, Qiu Y, Tao W Q. Heat transfer and friction of molten salt and supercritical CO_2 flowing in an airfoil channel of a printed circuit heat exchanger. Int J Heat Mass Tran 2020;150:119006.

[20] Zhao Z, Zhang Y , Chen X , Ma X, Yang S, Li S. Experimental and numerical investigation of thermal-hydraulic performance of supercritical nitrogen in airfoil fin printed circuit heat exchanger. Appl Therm Eng 2020;168:114829.

[21] Chen F, Zhang L, Huai X, Li J, Zhang H, Liu Z. Comprehensive performance comparison of airfoil fin PCHEs with NACA 00XX series airfoil. Nucl Eng Des 2017;315:42-50.

[22] Cui X, Guo J, Huai X, Cheng K, Zhang H, Xiang M. Numerical study on novel airfoil fins for printed circuit heat exchanger using supercritical CO_2. Int J Heat Mass Tran 2018;121:354-366.

[23] Han Z X, Guo J, Zhang H, Chen J, Huai X, Cui X. Experimental and numerical studies on novel airfoil fins heat exchanger in flue gas heat recovery system. Appl Therm Eng 2021;192:116939.

[24] Zhang H, Guo J, Cui X, Zhou J, Huai X, Zhang H, Cheng K, Han Z. Experimental and numerical investigations of thermal-hydraulic characteristics in a novel airfoil fin heat exchanger. Int J Heat Mass Tran 2021;175:121333.

[25] Guo Z Y, Tao W Q, Shah R K. The field synergy (coordination) principle and its applications in enhancing single phase convective heat transfer. Int J Heat Mass Tran 2005;48:1797-1807.

[26] Li F, Zhu W, He H. Numerical optimization on microchannel flow and heat transfer performance based on field synergy principle. Int J Heat Mass Tran 2019;130:375-385.

[27] Sun X Y, Hua L J, Dai Y J, Ge T S, Wang R Z. Field synergy analysis on heat and moisture transfer processes of desiccant coated heat exchanger. Int J Therm Sci 2021;164:106889.

[28] Li F, Zhu W, He H. Field synergy analysis on flow and heat transfer characteristics of nanofluid in microchannel with non-uniform cavities configuration. Int J Heat Mass Tran 2019;144:118617.

[29] Tao Y B, He Y L, Huang J, Wu Z G, Tao W Q. Three-dimensional numerical study of wavy fin-and-tube heat exchangers and field synergy principle analysis. Int J Heat Mass Tran 2007;50:1163-1175.

[30] Guo J, Huai X. Numerical investigation of helically coiled tube from the viewpoint of field synergy principle. Appl Therm Eng 2016;98:137-143.

[31] Liu Y P, Wang Y, Huang D G. Supercritical CO_2 Brayton cycle: A state-of-the-art review. Energy 2019;189:115900.

[32] Chu W X, Li X H, Ma T, Zeng M, Wang Q W. Heat transfer and pressure drop performance of printed circuit heat exchanger with different fin structures (in Chinese). Chin Sci Bull 2017;62:1788–1794.

[33] Ma T, Xin F, Li L, Xu X, Chen Y, Wang Q. Effect of fin-endwall fillet on thermal hydraulic performance of airfoil printed circuit heat exchanger. Appl Therm Eng 2015;89:1087–1095.

[34] Fu Q, Ding J, Lao J, Wang W, Lu J. Thermal-hydraulic performance of printed circuit heat exchanger with supercritical carbon dioxide airfoil fin passage and molten salt straight passage. Appl Energ 2019;247:594–604.

[35] NIST Web-Page, From: http://webbook.nist.gov/chemistry/fluid.

Table captions

Table 1. Numerical model validation with experimental data [12].

Table 2. Size data of the cold fluid channels.

Table 3. Case data of the cold fluid channel mass flow rate and *Re*.

Table 4. Field synergy numbers of three channels (cold-side inlet mass flow rate is 1.8912g/s).

Figure captions

Fig. 1. The physical model of the airfoil fin PCHE. (a) Geometric parameters of airfoil fin arrangement (Channel 1). (b) Channel arrangement and configuration. (c) Geometry and dimensions of hot and cold channels.

Fig. 2. Velocity field and temperature field of s-CO$_2$ in Channel 1 (s-CO$_2$ mass flow rate is 1.4184g/s). (a) Velocity. (b) Temperature.

Fig. 3. The proposed novel PCHE channel structures. (a) Channel 2. (b) Channel 3.

Fig. 4. Element channel for calculating the hydraulic diameter.

Fig. 5. Mesh independence test.

Fig. 6. Overall performances of three cold fluid channels with Reynold number. (a) Overall Nusselt number. (b) Overall Fanning friction factor. (c) Performance evaluation criterion.

Fig. 7. The distributions of velocity in the three types of channels. (a) Case 1. (b) Case 2. (c) Case 3.

Fig. 8. The distributions of temperature in the three types of channels. (a) Case 1. (b) Case 2. (c) Case 3.

Fig. 9. The local zones of Channel 1.

Fig. 10. The distributions of local parameters at the cross-sectional planes of three cold fluid

channels. (a) Local Reynold numbers. (b) Local Nusselt numbers. (c) Local *f* factors.

Fig. 11. Local field synergy angle of different channels.